ADVANCED ENERGY MATERIALS
www.advenergymat.de

Correlating Macro and Atomic Structure with Elastic Properties and Ionic Transport of Glassy Li_2S-P_2S_5 (LPS) Solid Electrolyte for Solid-State Li Metal Batteries

*Regina Garcia-Mendez, Jeffrey G. Smith, Joerg C. Neuefeind, Donald J. Siegel, and Jeff Sakamoto**

A combination of high ionic conductivity and facile processing suggest that sulfide-based materials are promising solid electrolytes that have the potential to enable Li metal batteries. Although the Li_2S-P_2S_5 (LPS) family of compounds exhibit desirable characteristics, it is known that Li metal preferentially propagates through microstructural defects, such as particle boundaries and/or pores. Herein, it is demonstrated that a near theoretical density (98% relative density) LPS 75-25 glassy electrolyte exhibiting high ionic conductivity can be achieved by optimizing the molding pressure and temperature. The optimal molding pressure reduces porosity and particle boundaries while preserving the preferred amorphous structure. Moreover, molecular rearrangements and favorable Li coordination environments for conduction are attained. Consequently, the Young's Modulus approximately doubles (30 GPa) and the ionic conductivity increases by a factor of five (1.1 mS cm^{-1}) compared to conventional room temperature molding conditions. It is believed that this study can provide mechanistic insight into processing-structure-property relationships that can be used as a guide to tune microstructural defects/properties that have been identified to have an effect on the maximum charging current that a solid electrolyte can withstand during cycling without short-circuiting.

1. Introduction

The goal to achieve widespread adoption of electric vehicles has accelerated the development of solid electrolytes for all-solid-state batteries (ASSBs).[1] ASSBs have garnered interest since they offer the potential for improved safety and energy density compared to lithium-ion batteries. To realize these advantages, the nonflammable solid electrolyte would replace the flammable liquid electrolyte and Li metal would replace carbon anodes to reduce cell volume and weight.[2] As a result, about 100% higher energy densities could be achieved compared to conventional Li-ion batteries.[3,4] Sulfide-based electrolytes with adequate ionic conductivity, low interfacial resistance against electrodes, and low processing cost make them one of the most promising inorganic solid electrolyte materials that could enable ASSBs.[5] However, despite the development of different compositions through different synthesis techniques in the Li_2S-P_2S_5 (LPS) family,[6–10] the successful transition to Li metal with relevant charging rates (≥3 mA cm^{-2} at room temperature) has not been realized.

It has been reported that microstructural defects, such as grain boundaries and/or pores can play a role in determining the maximum charging rate (or critical current density, CCD) a solid electrolyte can withstand without Li penetration.[11,12] Thus, a glassy, dense microstructure may be preferred for ASSB applications. In previous work,[13] the densification behavior or LPS 75-25 was studied as a function of temperature (25–300 °C) at fixed pressure (47 MPa). It was determined that crystallization of the thio-LiSICON III analog phase occurred between 170 and 250 °C. Moreover, the relative density was more or less invariant of densification temperature (≈80% RD; calculated dividing the geometrical density by its theoretical density in the amorphous phase: 1.88 g cm^{-3}).[14] While in our previous study, the maximum hot-pressing pressure (47 MPa) was limited by the mechanical integrity of the molding die, we recently developed capabilities to increase pressure to achieve 360 MPa. With this new capability, the current study compliments our previous study by investigating the densification behavior of LPS 75-25 as a function of pressure at fixed temperature. The pressure ranged between 47 and 360 MPa and the temperature was fixed at the glass transition temperature (T_{glass}). We hypothesize that by increasing the molding pressure the relative density will increase. Furthermore, the simultaneous application of

R. Garcia-Mendez, Prof. D. J. Siegel, Prof. J. Sakamoto
Department of Materials Science and Engineering
University of Michigan
Ann Arbor, MI 48109, USA
E-mail: jeffsaka@umich.edu
Dr. J. G. Smith, Prof. D. J. Siegel, Prof. J. Sakamoto
Department of Mechanical Engineering
University of Michigan
Ann Arbor, MI 48109, USA
Dr. J. C. Neuefeind
Spallation Neutron Source
Oak Ridge National Laboratory
Oak Ridge, TN 37831, USA
Prof. J. Sakamoto
University of Michigan
Ann Arbor, MI 48109, USA
The ORCID identification number(s) for the author(s) of this article can be found under https://doi.org/10.1002/aenm.202000335.

DOI: 10.1002/aenm.202000335

pressure at T_{glass} during processing will dramatically reduce the elastic modulus, thereby increasing flow to facilitate densification. It will be shown that the samples obtained through this processing approach indeed have relative densities up to 98% and that significant enhancement to the ionic conductivity and an increase in elastic modulus were observed. We believe the outcomes of this study can provide mechanistic insight into processing-structure-property relationships to improve the feasibility of LPS-based solid-state battery technology.

2. Results and Discussion

2.1. Materials Characterization

2.1.1. Effect of Processing Temperature on LPS 75-25 Densification

Typically, differential scanning calorimetry (DSC) is used to measure T_{glass}; however, thermomechanical analysis (TMA) was used because DSC relies on measuring changes in heat capacity and the change in heat capacity associated for LPS during this transition is not sufficient to determine T_{glass}. TMA measures the change in dimensions as a function of temperature to determine the transition from a vitreous solid to an amorphous liquid. The dimension change versus temperature and corresponding derivative data for a cold pressed LPS 75-25 pellet are shown in **Figure 1**a. The T_{glass} is more precisely described as a transformation range,[15] thus, it was determined that the onset for this transformation started at 200.0 ± 0.1 °C with and upper limit at 213.6 ± 0.1 °C. The largest change in dimension occurred at 204.6 ± 0.1 °C as observed from the derivative dimension change trace in Figure 1a. A heating rate of 0.7 °C min^{-1} was used to measure T_{glass} to match the heating rate used during the densification in this study. The T_{glass} is similar, but lower compared to the T_{glass} of 220 °C for LPS 70-30 measured by Minami et al. and Tatsumisago et al.[8,16] This difference is attributed to the difference in composition, but mainly to the higher heating rate used. Both Minami et al. and Tatsumisago et al. used a heating rate of 10 °C min^{-1}, compared to 0.7 °C min^{-1} for this study. Since T_{glass} refers to a structural relaxation transition, it depends on kinetic factors as proposed by the Bartenev–Ritland equation.[15] The structural relaxation time is inversely proportional to the cooling/heating rate. Thus, LPS 75-25 with a slower heating rate than 70-30 will exhibit the structural relaxation sooner (lower temperature) than the 70-30 LPS with a faster heating rate. More importantly, for processing purposes, a slower heating rate allows sufficient time for atoms to rearrange resulting in a denser glass.[17]

$T_{crystallization}$ was measured using DSC (Figure 1b) heating at 0.7 °C min^{-1} for cold pressed (360 MPa) and hot-pressed (200 °C, 270 MPa). Again, 0.7 °C min^{-1} was used to match the heating rate during densification. For both samples, $T_{crystallization}$ was determined to be 223.7 ± 0.6 °C, which is in excellent agreement with previous work.[13] Subtle endotherms/exotherms were observed at ≈100 °C in both samples and are believed to be associated with traces of moisture in the purging gas, since according to specifications, still contains <5 ppm of moisture. This is believed to be the case rather than resulting from moisture in the sample/pan given that hermetic pans were used and sealed in a dry (<0.5 ppm H_2O) Ar glovebox in addition to storing the pans in a vacuum oven at 120 °C. The heat capacity at constant pressure showed no appreciable change after hot-pressing at 200 °C, 270 MPa, confirming that no or negligible crystallization occurred. Nevertheless, there was a 23% decrease in the latent heat of crystallization after hot-pressing (85.35 J g^{-1}; and Figure S1, Supporting Information), suggesting that hot-pressing while maintaining the amorphous phase results in a slightly more thermodynamically stable structure compared to the amorphous cold-pressed LPS given that the calculated latent heat of crystallization was normalized by mass. From Figure 1, several observations can be made. First, TMA determined that the T_{glass} was between 200.0 ± 0.1 and 213.6 ± 0.1 C °C. Thus, to increase flow during densification, by heating above T_{glass}, the temperature selected was 200 °C and used throughout this study for all hot-pressed samples. Whereas in our previous study, hot pressing was conducted at 130, 150, 170, 190, 250, and 300 °C at a fixed pressure of 47 MPa, thereby excluding the temperature range between T_{glass} and $T_{crystallization}$.[13] Second, DSC determined that the $T_{crystallization}$ was 223.7 ± 0.6 °C and did not change after hot-pressing at 270 MPa and 200 °C. This confirms that hot-pressing LPS at 270 MPa and 200 °C did not cause crystallization. Taken together, the TMA and DSC analyses determined the upper ($T_{crystallization}$) and lower (T_{glass}) bound temperatures for processing. By hot-pressing between these salient temperatures, we believed significantly higher densities can be achieved. Moreover, it was found that hot-pressing in this temperature regime, and at higher pressures compared to the previous study,[13] had beneficial and unexpected consequences

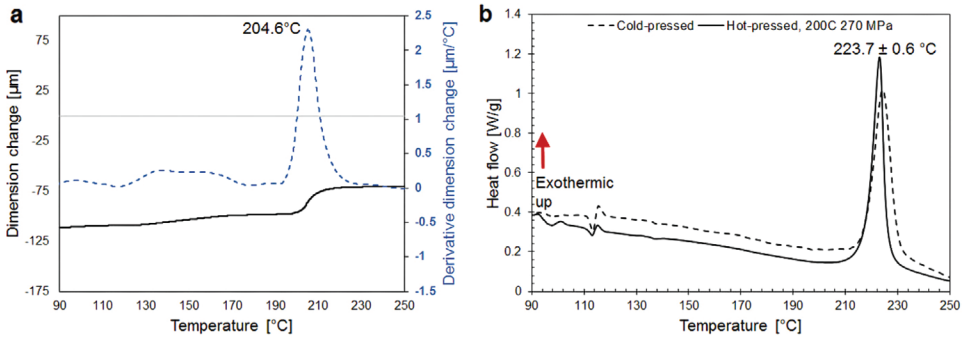

Figure 1. Measurement of glass transition and crystallization temperature of LPS 75-25 via a) thermomechanical analysis (TMA) and b) Differential Scanning calorimetry (DSC), respectively. Heating rate on both tests was 0.7 °C min^{-1}, same used for densification.

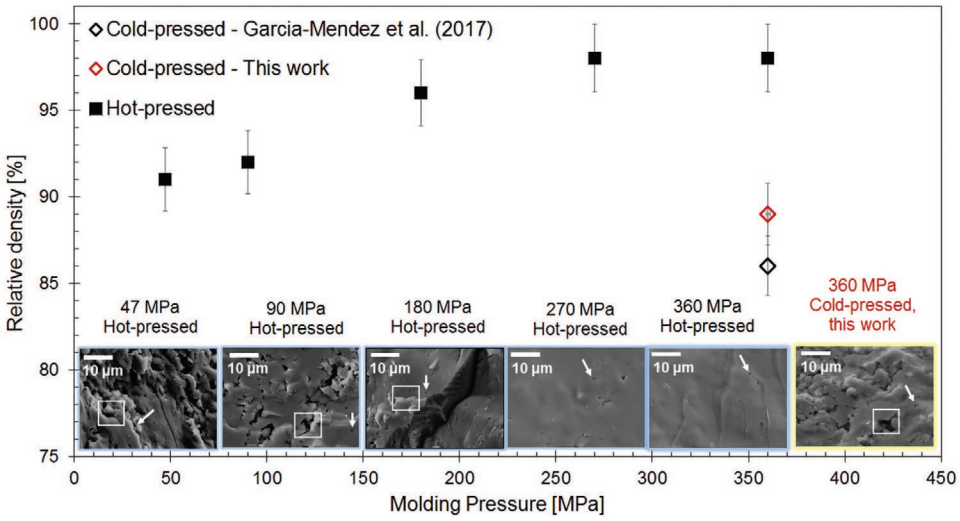

Figure 2. Relative density as a function of molding pressure of LPS 75-25 with a theoretical density of 1.88 g cm^{-3}. Fracture surfaces and density measurements of LPS 75-25. Insets of Secondary Electron Microscope (SEM) images correspond to fracture surfaces with particle boundaries and porosity highlighted using white boxes and arrows, respectively.

to the atomic packing factor and the physical and electrical properties.

2.1.2. Microstructural Analysis

Our previous work reported that the LPS geometric density values, and consequently, its relative density (RD) values were invariant to processing temperature from 130 to 300 °C at fixed pressure (47 MPa).[13] The lack of densification is believed to be attributed to the lack of viscous flow, yielding samples with ≈80% RD compared to its theoretical density in the amorphous phase (1.88 g cm^{-3}),[14] regardless of the hot-pressing temperature. In this study, dramatically different densification is observed (**Figure 2**). The RD clearly increases with increasing pressure (at the fixed temperature of 200 °C). Pressing at room temperature, or cold-pressing, at 360 MPa achieves 89 ± 2% RD, which is consistent with the theoretical calculations conducted in this study (discussed in Section 2.2), in addition with other reports in literature.[14,18] This represents a 3% increase in mean RD compared to our previous study (86 ± 2% RD).[13] However, the changes observed are within the detection limits of the instrument. For all other samples the hot-pressing temperature was 200 °C. At 47 and 90 MPa, the RD were 91 ± 2% and 92 ± 2%, respectively. It was at pressures of 180 MPa and above that a significant increase in RD was achieved and noticeable change in microstructure (fracture surfaces) was observed. For example, hot-pressing at 47 and 90 MPa produced microstructures consisting of discernable particle boundaries and porosity (Figure 2). In comparison, when pressing at 180 MPa, the particle boundaries are more-or-less absent and the fraction and size of the porosity is noticeably lower. Increasing from 90 to 180 MPa also resulted in the largest increase in RD (≈4%) compared to the other increments in pressure from 180 to 270 and 270 to 360 MPa. Furthermore, the fracture surfaces of samples hot-pressed at and above 270 MPa are consistent with a glassy fracture with no evidence of particle boundaries and negligible porosity. From the relative density and fracture surface analysis, it is believed that the decrease in porosity and lack of discernable particle boundaries or glassy fracture surfaces, suggests that hot-pressing at T_{glass} and at pressures > ≈180 MPa produces a microstructure resembling a typical melt-processed glass. However, to confirm that crystallization on the macroscopic scale did not occur along with densification, X-ray diffraction was conducted.

2.1.3. Suppression of Heterogeneous Nucleation

To determine if crystallization occurred during densification at 200 °C between 47 and 360 MPa X-ray diffraction was conducted (**Figure 3**). With the exception of the sample pressed at 47 MPa, all samples lacked evidence of crystallinity and resembled the diffraction pattern of cold-pressed LPS. As the molding pressure for hot-pressing decreased from 360 to 47 MPa, gradual intensification of diffraction peaks in the X-ray spectrum corresponding with the crystallization of the thio-LISICON III analog was evident.[19] This metastable crystalline phase was also observed in our previous work where precipitation from the mother glass was seen in LPS hot-pressed between 170 and 250 °C at 47 MPa.[13] The samples obtained were glass-ceramics under those processing conditions. The presence of crystalline phases below the glass transition and crystallization temperature was unexpected since the T_{glass} corresponds to the transition in which atoms rearrange starting as a vitreous solid transforming into an amorphous liquid followed by crystallization. As explained by nucleation and growth theory, the crystallization process of glassy materials consists of nucleation and crystal growth stages.[17] Typically, the formation of nuclei is around the onset of the $T_{crystallization}$ followed grain growth; however, pores and free surfaces can act as heterogeneous nucleation sites favoring crystal growth.[17] These regions could act as preferred nucleation sites since they have higher free energy, thus, facilitating nucleation and growth

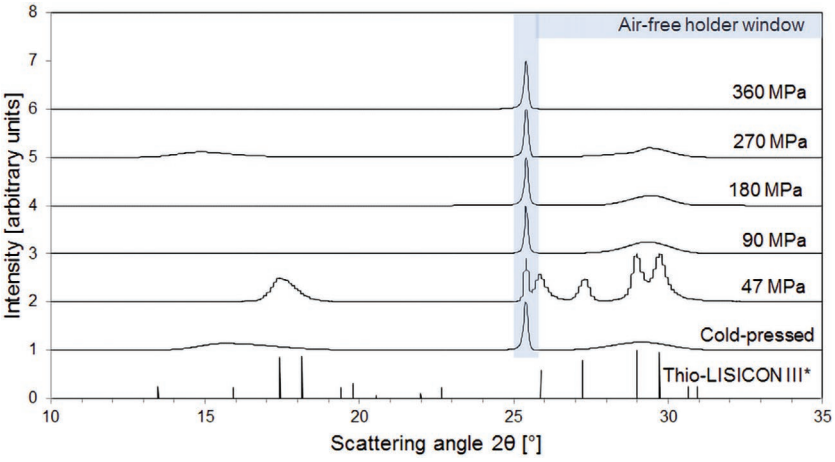

Figure 3. X-ray diffraction patterns of LPS 75-25 as a function of molding pressure. The thio-LISICON III X-ray diffraction pattern was based on data from ref. [15].

of the crystalline phase. Indeed, the samples that showed the presence of the thio-LISICON III analog crystalline phase had a high-volume fraction of porosity (9–20%) and free surfaces, both acting as heterogeneous nucleation sites favoring crystal growth. This was also manifested indirectly on the higher latent heat of crystallization measured by DSC on the cold-pressed sample compared to the 98% dense hot-pressed sample at 200 °C, 270 MPa (Figure S1a,b, Supporting Information). We believe that the lack of pores or free surfaces on the near to theoretical density samples reduces strain energy that suppresses the nucleation or growth of the crystalline or metastable crystalline phases. In agreement, the samples that exhibited RD ≥ 98%, showed little to no metastable crystalline phase based on the X-ray diffraction measurements. In addition, the thermodynamic barrier to nucleation is suppressed as the contact angle between the crystalline nuclei and the amorphous phase decreases.[17] We believe the higher the degree of densification, the lower the contact angle is obtained between the crystalline nuclei and amorphous phase suppressing crystallization. From the X-ray diffraction pattern, the broad peak observed on the sample hot-pressed at 270 MPa along with the crystallization peak observed from DSC at 223.7 ± 0.6 °C, corroborates that a glassy sample can be attained by hot-pressing at 200 °C.

2.2. Mechanical Properties

The elastic constants and hardness were measured using a combination of ultrasonic velocity measurements and nanoindentation experiments (**Figure 4**). Both techniques were used to probe the LPS mechanical properties at different length scales; the ultrasonic velocity measurements to acquire bulk properties and nanoindentation for localized, single-particle properties. Longitudinal and shear wave speeds were used to determine the Young's (E) and Shear (G) Moduli using Equations (2) and (3) (see the Experimental Section).

The E of cold-pressed LPS at 360 MPa was measured to be 13.7 ± 1.3 GPa, in agreement with Sakuda et al. measurements.[18] As expected, this value is much lower than the E reported for Li-ion conducting oxide glasses, such as Li_2O-P_2O_5 50-50, with an E of 39.6 GPa.[20] This value would be anticipated to be even higher for a 75-25 composition as observed with sulfide glasses as the glass modifier concentration is increased.[21] The higher moduli observed in oxide glasses compared to sulfide glasses lies in the higher bonding dissociation energies resulting in a more rigid glass network (P-S: 442 kJ mol^{-1}, Li-S: 313 kJ mol^{-1}, P-O: 589 kJ mol^{-1}, Li-O: 341 kJ mol^{-1}), in addition to a higher packing density.[22]

Despite using lower pressure compared to what is typically used for cold-pressing (e.g., 360 MPa), Hot-pressing LPS at 200 °C at 47 and 90 MPa, resulted in a greater E (16.7 ± 0.6 and 16.5 ± 0.5 GPa, respectively) compared to the cold-pressed pellet (13.2 ± 0.95 GPa). We believe this is a consequence of increasing viscous flow that results from heating at T_{glass}, which lowers the volume fraction of porosity as shown via electron microscopy and density measurements in Section 2.1.2. This behavior is consistent with the exponential relationship between E and the volume fraction of porosity reported by Rice et al.[23] (Figure 4c). The increase in E is believed to be a result of the change in volume fraction of porosity of 3–4% compared to the cold-pressed sample rather than the presence of the metastable crystalline phase detected via X-ray diffraction (XRD) for the sample hot-pressed at 47 MPa. The presence of the thio-LISICON III analog phase is not believed to correlate with the increase in E given that the difference in E for both hot-pressed samples is negligible and the change in density between both samples was only of 1%. Additionally, crystalline phases in the LPS system would be expected to exhibit higher E values compared to the amorphous phase as demonstrated later in the calculated elastic properties. This suggests that the volume fraction of metastable crystalline phase is not sufficient to increase E to a higher extent than the reduction in volume fraction of porosity (**Table 1**). In other words, the volume fraction of metastable crystalline phase is not sufficient to increase E or G at the bulk scale as it was reflected from the time of flight measured for the longitudinal and shear waves for both samples during ultrasonic velocity measurements.

Hot-pressing LPS from 90 to 180 MPa led to a significant increase in Young's Modulus, E, reaching 30.9 ± 0.5 GPa. This change in elastic properties agrees well with the above finding that particle boundaries and porosity decreased considerably by hot-pressing at and above 180 MPa, as observed in the scanning electron microscopy (SEM) fractographs (Figure 2). However, a decrease in the volume fraction of porosity alone cannot completely explain the increase in E (as it is also evident from the exponential fit shown in Figure 4c). We believe the slight deviation from the expected exponential relationship is attributed to changes on the intramolecular level (intermediate-range order) for the samples hot-pressed ≥ 180 MPa. It is known that more interconnected molecular organizations, such as a 3D network, can lead to a significant increase in E.[24] Thus, to evaluate the local coordination of these disordered materials, pair distribution functions (PDF) were collected via neutron diffraction (**Figure 5**c). In the case of

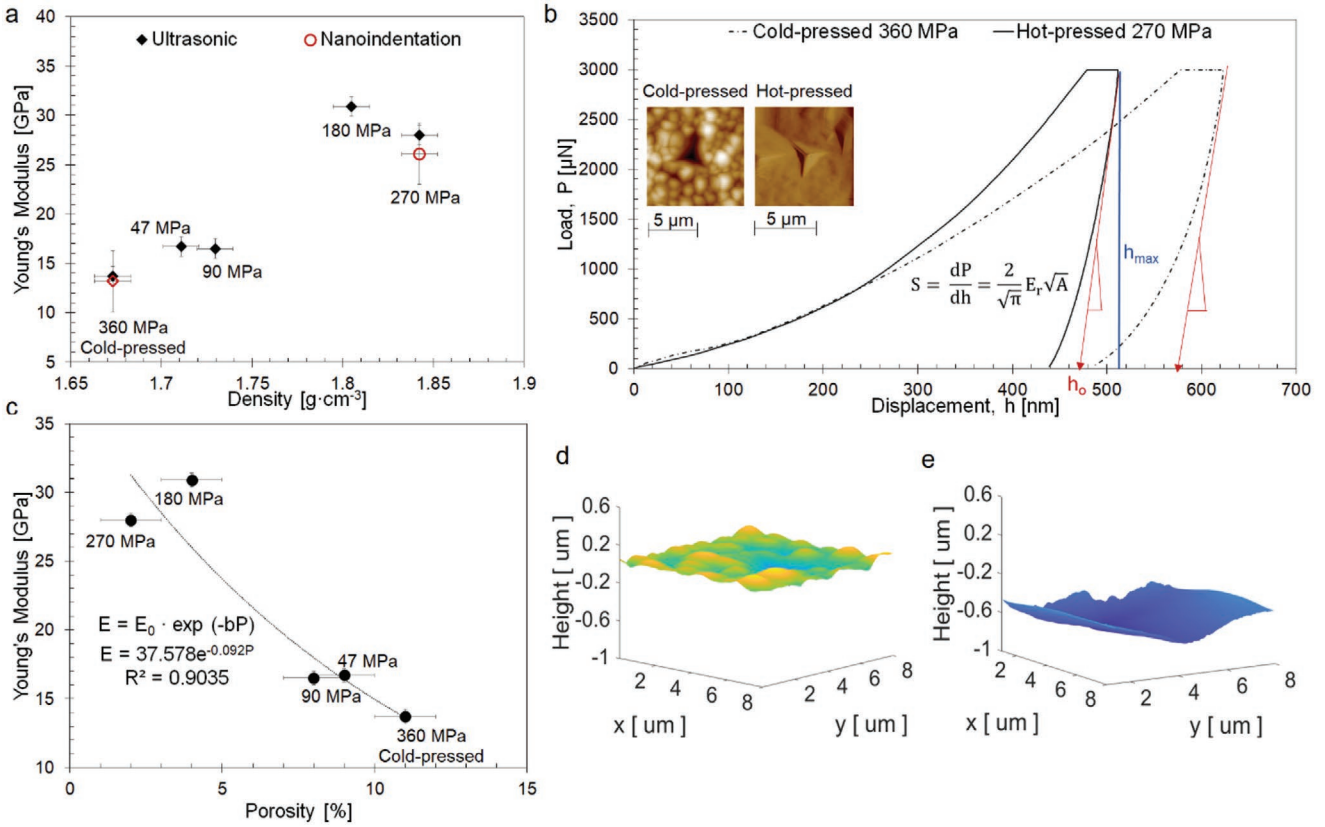

Figure 4. Elastic and plastic behavior of LPS 75-25. Young's Moduli of LPS 75-25 as a function of molding pressure via ultrasonic velocity measurements and nanoindentation a,b). Inset in (b) shows the Atomic Force Microscope (AFM) 2D images acquired from cold-pressed and hot-pressed LPS at 270 MPa 200 °C. c) Young's Moduli as a function of porosity where E_0 denotes the Young's Modulus at 0 porosity, P the volume fraction of porosity, and b is a dimensionless constant. LPS Atomic Force Microscopy (AFM) 3D maps of d) cold-pressed sample and e) hot-pressed sample at 270 MPa, 200 °C.

glasses with covalently bonded elements, the mean coordination number can be used to correlate physical properties to structural changes. A higher mean coordination number would correspond to a more interconnected molecular organization resulting in a higher E.[24] From the spectra collected, it was observed that the sample hot-pressed at 270 MPa, E of 28.0 ± 0.6 GPa, showed a ≈20% increase in peak intensity compared to the sample hot-pressed at 47 and 90 MPa (E of 16.7 ± 0.6 and 16.5 ± 0.5 GPa, respectively), mostly on the Li–S pairs. This increase is closely related to the change in the coordination environment of the Li ions,[25] but more importantly, suggesting a more interconnected arrangement between Li and S for the samples hot-pressed at 180 and 270 MPa resulting in larger elastic constants.

A slight decrease in E was observed for the LPS hot-pressed at 270 MPa (28.0 ± 0.6 GPa) and the sample hot-pressed at 360 MPa was not sufficiently strong to withstand handling and fractured upon instrumentation. Residual stress in uniaxially hot-pressed materials are known to occur due to differences in thermal expansion coefficients between the molding die and the powder, frictional forces between the wall of the die, and the extraction process.[26] It is for these reasons that we believe the samples hot-pressed at 270 and 360 MPa are the most likely to have the highest residual stress among all samples. Anecdotally, the samples hot pressed at 270 and 360 MPa were relatively weak and brittle, consistent with the presence of residual stress. Thus, the slight decrease in E (2 GPa), by increasing the hot-pressing pressure from 180 to 270 MPa, is attributed to the presence of microcracks that attenuated the acoustic wave speed. Similar behavior is observed for the Shear modulus (Figure S2, Supporting Information), which is expected since glasses are elastically isotropic. To minimize the impact that particle boundaries and porosity may have on the measurement of E, nanoindentation was conducted. The E values obtained via nanoindentation for the cold-pressed sample and hot-pressed at 270 MPa (13.2 ± 1.0 and 26.1 ± 3.1 GPa, respectively, load vs displacement curves shown in Figure 4b) are in good agreement with the bulk-type measurements (13.7 ± 1.3 and 28.0 ± 0.6 GPa, respectively). These data further suggest that the changes in elastic properties measured were related to atomic/molecular changes rather than just changes in porosity alone. The slight reduction in E from nanoindentation for the hot-pressed sample at 270 MPa could be due to the localized nature of the measurements that could have included some indentations that were close to microcracks, thus reducing those particular E values. The Hardness H values determined via nanoindentation for the cold-pressed and hot-pressed at 270 MPa showed the behavior expected for reduced volume fraction porosity; an increase in hardness, going from 0.29 ± 0.04 to 0.65 ± 0.07 GPa (89–98% relative density) as shown in Figure S2 (Supporting Information). The corresponding shear moduli for all samples

Table 1. Calculated elastic properties of Li_3PS_4 glass and of related crystalline materials (γ-Li_3PS_4, β-Li_3PS_4, and $Li_7P_3S_{11}$) as a function of density, ρ. The elastic constants C_{ij}, bulk modulus B, shear modulus G, and Young's modulus E have units of GPa.

	ρ [g cm^{-3}]	B [GPa]	G [GPa]	E [GPa]	ν	C_{ij}					
glass-Li_3PS_4	1.55	9.82	5.10	13.04	0.28	12.7	6.4	6.8	0.4	0.0	−1.5
						6.4	15.7	7.3	1.7	−1.0	−0.9
						6.8	7.3	19.7	0.8	−1.2	0.1
						0.4	1.7	−1.2	5.5	0.4	−0.3
						0.0	−1.0	−1.2	0.4	5.8	0.4
						−1.5	−0.9	0.1	−0.3	0.4	6.2
	1.65	14.26	6.75	17.49	0.30	20.6	9.7	9.8	−0.4	−0.2	−0.5
						9.7	25.2	10.0	1.3	−0.1	−0.9
						9.8	10.0	24.1	0.4	0.2	−0.3
						−0.4	1.3	0.2	7.4	−0.6	0.0
						−0.2	−0.1	0.2	−0.6	6.6	0.3
						−0.5	−0.9	−0.3	0.0	0.3	6.8
	1.76	16.93	6.61	17.54	0.33	24.4	12.0	13.4	−1.3	−0.1	0.7
						12.0	26.8	12.0	−0.8	0.1	2.0
						13.4	12.0	27.7	1.1	−3.5	0.6
						−1.3	−0.8	−3.5	8.3	−0.7	0.9
						−0.1	0.1	−3.5	−0.7	7.2	−0.2
						0.7	2.0	0.6	0.9	−0.2	5.1
	2.42	50.70	16.27	44.10	0.36	71.8	37.2	41.7	−0.5	−0.2	−0.3
						37.2	71.5	41.2	−1.3	0.7	−0.1
						41.7	41.2	71.0	0.5	6.1	1.8
						−0.5	−1.3	6.1	18.9	0.3	−0.1
						−0.2	0.7	6.1	0.3	17.6	−0.4
						−0.3	−0.1	1.8	−0.1	−0.4	14.4
γ-Li_3PS_4	1.87	31.90	13.02	34.40	0.32						
β-Li_3PS_4	1.80	21.72	11.14	28.55	0.28						
$Li_7P_3S_{11}$	1.80	23.43	9.32	24.69	0.32						

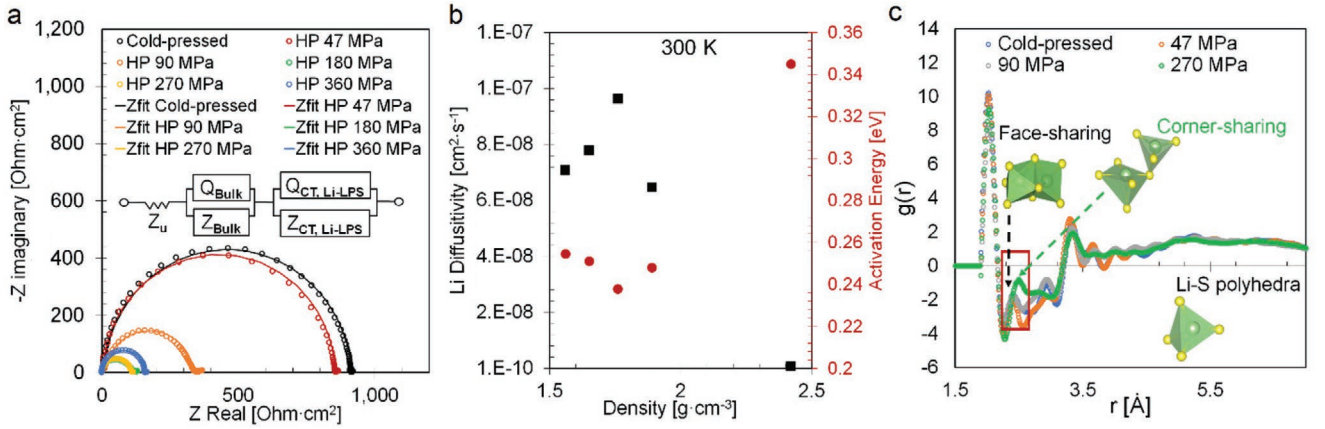

Figure 5. Measured and calculated ionic transport of LPS 75-25 a) Electrochemical Impedance Spectroscopy (EIS) spectra of Li-LPS-Li cells at room temperature at 3.5 MPa with their corresponding fit. b) Calculated lithium self-diffusivity at 300 K and activation energy as a function of density. c) Pair distribution functions g(r) of LPS 75-25 obtained via time-of-flight neutron diffraction for samples processed at different molding pressures showing a shift on the Li–S pair from a face-sharing to a corner-sharing configuration when hot-pressing LPS at 270 MPa, 200C.

Table 2. Density, mechanical properties, and ionic conductivity of LPS 75-25 as a function of molding pressure.

Molding Pressure [MPa]	Molding temperature [°C]	Density [±0.01 g cm^{-3}]	RMS roughness	Ultrasonic velocity		Nanoindentation		Ionic conductivity @25 °C [mS cm^{-1}]
				Shear Modulus [GPa]	Young's Modulus [GPa]	Young's Modulus [GPa]	Hardness [GPa]	
47	200	1.71		6.4 ± 0.2	16.7 ± 0.6			0.3
90	200	1.73		6.3 ± 0.2	16.5 ± 0.5			0.4
180	200	1.80		11.8 ± 0.2	30.9 ± 0.5			1
270	200	1.84	35.03 ± 13.20	10.7 ± 0.7	28.0 ± 0.6	26.1 ± 3.1	0.65 ± 0.07	1.1
360	200	1.86		—	—			0.8
360	25	1.67	30.03 ± 1.24	5.3 ± 0.5	13.7 ± 1.3	13.2 ± 1.0	0.29 ± 0.04	0.2

including the root-mean-square (RMS) roughness measured via atomic force microscopy (AFM) for the cold-pressed and hot-pressed at 270 MPa 200 °C are listed in **Table 2**.

The calculated elastic coefficients, and moduli of LPS 75-25 as a function of density are shown in Table 1. The density of the melt quenched to 300 K under atmospheric pressure was 1.55 g cm^{-3}; Sakuda et al. measured a cold pressed density of 1.45 g cm^{-3} at 180 MPa.[18] Hydrostatic pressure applied at 360 MPa during ab initio molecular dynamics (AIMD) resulted in a higher density of 1.65 g cm^{-3}, which is in good agreement with the density of the cold-pressed samples reported here at 360 MPa (1.67 g cm^{-3}, see Table 2). Increasing the hydrostatic pressure from 0.1 to 360 MPa within the simulation increased all of the bulk, shear and *E*, from 9.8 to 14.3 GPa, 5.1 to 6.8 GPa, and 13.0 to 17.5 GPa, respectively. Further increasing the density to 1.76 g cm^{-3} (corresponding to $P = 1$ GPa) yielded insignificant changes to the shear and *E*. This density lies within the density experimental values of the samples hot-pressed at 90 and 180 MPa (1.73 and 1.80 g cm^{-3}, respectively), where the significant increase in *E* was also observed. The calculated elastic moduli of the glass for the densities of 1.67–1.76 g cm^{-3} are consistent with the measured values in this work (Table 2) and those of Sakuda et al.[18] At these densities, the calculated bulk, shear, and *E* are approximately half the moduli of the related crystalline phases, γ- and β-Li_3PS_4, and of $Li_7P_3S_{11}$. (The former phases include an ordered arrangement of PS_4 anions; $Li_7P_3S_{11}$ includes both PS_4 and P_2S_7 anions.) Finally, calculations performed at the highest density investigated, 2.42 g cm^{-3} (corresponding to $P = 10$ GPa) resulted in moduli that exceed those of the crystalline materials.

Additionally, topographic maps were acquired via AFM of the cold-pressed sample and hot-pressed sample at 200 °C and 270 MPa (Figure 4d,e). The lack of discernable particles within the microstructure for the hot-pressed sample is in agreement that a glassy material was obtained, resembling a melt-processed glass. Furthermore, the cold-pressed sample map still shows discernable particles within the microstructure as expected, shown as peaks and valleys. Although the RMS roughness values measured for each did not vary significantly (30.03 ± 1.24 for the cold-pressed sample and 35.03 ± 13.20 for the hot-pressed sample), the peaks and valleys found in the hot-pressed sample are taller and deeper than the cold-pressed sample. Also, the distance that separates each peak is larger for the hot-pressed sample. The repercussions to this during cell assembly need to be considered. It is known that Li metal exhibits significant creep at room temperature,[27,28] thus, load above the yield strength of Li[29] can facilitate contact between electrode and electrolyte as it can be observed in Figure S3 (Supporting Information) for all samples when assembling Li|LPS|Li symmetric cells. Therefore, the values selected when measuring ionic conductivity in Section 2.3 were taken when the areal specific resistance for the bulk contribution did not show considerable change as a function of cell stack pressure. Ionic measurements were carried out to further investigate the relationship between structure and properties in this thiophosphate solid electrolyte.

2.3. Lithium Ionic Transport

The electrochemical impedance spectroscopy (EIS) spectra collected and fitted (Figure 5a and **Table 3**) showed that the

Table 3. Electrochemical impedance spectroscopy analysis of LPS processed at different molding pressures. The α-values account for deviation from the ideal pure capacitor behavior ($\alpha = 1$).[35]

Parameter	Cold-pressed	Hot-pressed, 47 MPa	Hot-pressed, 90 MPa	Hot-pressed, 180 MPa	Hot-pressed, 270 MPa	Hot-pressed, 360 MPa
Z_u [Ohm cm^2]	6.8	3.5	10.1	0.4	0.5	0.4
Q_{Bulk}, [F]	2.8×10^{-9}	2.4×10^{-9}	3.3×10^{-9}	2.0×10^{-9}	0.94×10^{-9}	0.93×10^{-9}
α_b	0.96	0.98	0.95	0.85	0.91	0.98
Z_{Bulk}, [Ohm cm^2]	907.9	852.1	326.7	112.6	109.3	158.3
$Q_{CT,\ Li\text{-}LPS}$ [F]	3.8×10^{-3}	1.8×10^{-3}	3.0×10^{-3}	4.1×10^{-3}	1.2×10^{-3}	6.2×10^{-3}
$\alpha_{CT,\ Li\text{-}LPS}$	0.90	0.97	0.82	0.95	0.94	0.87
$Z_{CT,\ Li\text{-}LPS}$[Ohm cm^2]	9	12.6	21.5	9.5	4.8	4.0

LPS cold-pressed (360 MPa) exhibits a room temperature ionic conductivity of 0.2 mS cm^{-1}, which is in good agreement with the values reported previously.[30,31] When hot-pressing the sample at 200 °C and 47 MPa resulting in a glass-ceramic, the ionic conductivity slightly increased to 0.3 mS cm^{-1}. This is expected with the presence of the thio-LISICON III analog phase detected via XRD measurements, since it has been reported to have a slightly higher ionic conductivity of 0.64 mS cm^{-1} at room temperature[30] enhancing the overall ionic transport within the glass–ceramic electrolyte. It has been seen that the ionic conductivity in Li thiophosphate materials depends not only on their structural order (crystalline vs amorphous), but also on the crystalline phase(s) that precipitate from the mother glass.[16,30–32] In the case of the amorphous LPS 75-25, an ionic conductivity of 0.32 mS cm^{-1} at room temperature has been reported[30,31] and upon heating (up to 250 °C), conductivities slightly higher, still on the 0.1 mS cm^{-1} range, have been observed due to the precipitation of the thio-LISICON III analog ($Li_{3.2}P_{0.96}S_4$) metastable crystalline phase.[13] This phase is not thermodynamically stable since upon further heating evolves into other crystalline phases, such as γ-Li_3PS_4, β- Li_3PS_4, and $Li_4P_2S_6$, all with a lower room temperature conductivity in the order of 1×10^{-3} mS cm^{-1}.[33,34]

From Figure 5a, it can be observed that the room temperature ionic conductivity of LPS 75-25 increased from 0.3 to 1.1 mS cm^{-1} when hot-pressing from 47 to 270 MPa (1.71–1.84 g cm^{-3}), and a slight decrease to 0.8 mS cm^{-1} when hot-pressing at 360 MPa (1.86 g cm^{-3}). To explain the changes observed, the impact of densification on the internal volume (void space) available for Li motion and Li diffusivity was quantified. Moreover, the anionic building units were identified via Raman since it is known that lithium is dynamically coupled to the reorientation and thermal vibration of the local anionic building units in thiophosphate glasses.[36] The Raman spectra (Figure S6, Supporting Information) showed *ortho*-thiophosphate species (PS_4^{3-}) as the dominant species at 421 ± 1 cm^{-1}, known to be responsible for the high ionic conductivity in Li thiophosphate glasses.[37] In addition, *hypo*-thiophosphate species ($P_2S_6^{4-}$) at around 380 cm^{-1} were detected, in agreement with Dietrich et al. for this composition.[37] The intensity of both signals were independent from the densification conditions, therefore, the concentration of PS_4^{3-} and $P_2S_6^{4-}$ are believed to be the same among all samples. Consequently, the fraction of anion polymorphs are not responsible for the changes in ionic transport observed in this study.

Regarding the volume available for Li migration, Figure S8 (Supporting Information) plots the relationship between the glass density and the characteristic dimensions for the channels (i.e., void space) available for Li migration within the glass. Earlier studies of ion migration in solids have shown that the size of the migration channel strongly correlates with ion mobility.[38] For example, Ichihashi et al.[38] have shown that ion migration is facilitated when the channel diameter is neither too small—a narrow bottleneck tends to block migration—nor too large. (In the latter case, the mobile species migrates along the pore surface.) Using the crystallographic topology analysis routines implemented in the Zeo++ code, Figure S8 (Supporting Information) demonstrates that, as expected, the diameters of both the largest included sphere (D_i) and the largest included sphere along the free sphere path (D_{if}) monotonically decrease with increasing density. (D_i describes the diameter of the largest pore found anywhere within the glass model, while D_{if} refers to the largest diameter along a channel that permeates the entire system, and which is everywhere large enough to accommodate Li+ migration.) From Figure 5b, the activation energy and diffusivity of Li are predicted to be minimized and maximized, respectively, for a density of 1.75 g cm^{-3}. The void space analysis in Figure S8 (Supporting Information) shows that at this density, $D_i = D_{if} = 3.1$ Å. This implies that the optimal channel size for Li migration in the LPS glass is ≈3.1 Å, and that this dimension is achieved for densities near 1.75 g cm^{-3}. Thus, the highest ionic conductivity would have been expected near such density. Experimentally, the highest ionic conductivity value of 1.1 mS cm^{-1} was observed at 1.84 g cm^{-3}. Even though there is a ≈5% deviation between predicted versus experimental values, it is reasonable to believe that the ionic transport changes observed as a function of density can be explained via theoretical calculations. When hot-pressing LPS 75-25 at 90 MPa a room temperature ionic conductivity of 0.4 mS cm^{-1} was observed. The change observed compared to the sample hot-pressed at 47 MPa is attributed mainly to increased diffusivity reflected as higher ionic conductivity according to the Nernst–Einstein equation.[39] AIMD calculations predicted that when going from 88% to 94% relative density (1.65–1.77 g cm^{-3}), the lithium self-diffusivity increases from 7.8×10^{-8} to 9.6×10^{-8} cm^2 s^{-1} at 300 K as shown in Figure 5b; and Table S1 (Supporting Information). Furthermore, activation energies for Li ion conduction are in agreement with the changes observed in lithium self-diffusivity; samples with higher lithium self-diffusivity exhibit a lower activation energy for Li ion conduction.

The largest change in ionic conductivity compared to the cold-pressed sample occurred when hot-pressing LPS at 180 and 270 MPa, resulting in 1.0 and 1.1 mS cm^{-1}, respectively. The increase in conductivity observed in the LPS hot-pressed at 180 and 270 MPa is also consistent with the microstructural changes (glassy fractures and nearly theoretical densities). Aside from the optimal channel size found for Li migration in LPS glass that facilitates ionic transport, the impact of densification on Li diffusivity for different Li coordination environments was quantified. It has been reported that Li-ions in thiophosphate glasses experience a range of different coordination environments.[36] Therefore, partial pair distribution functions (p-PDF) and total neutron weighted PDF, $G'(r)$ were simulated (Figure S4, Supporting Information) and compared to the experimental data acquired via neutron scattering. First, from the PDF obtained via neutron diffraction (Figure 5c), it was observed that the Li environment changes as a function of molding pressure. More specifically, shifts on the bond lengths for the Li–S pairs were measured. The sample hot-pressed at 270 MPa with highest ionic conductivity of 1.1 mS cm^{-1} showed a Li—S bond distance of 2.54 Å compared to a bond distance of 2.4 Å for the sample hot-pressed at 90 MPa (0.4 mS cm^{-1}). Even though the Li—Li bond lengths were not well defined to determine shifts, calculations determined that Li–S polyhedra exhibiting corner sharing show a Li—S bond length of 2.52 Å as opposed to a 2.43 Å bond length for Li–S polyhedra with a face-sharing configuration. Although the shift between Li–S pairs was not expected to increase as the molding pressure

increased, mechanical anisotropy has been reported for $Li_4P_2S_6$ via first-principles calculations.[40] Based on the Raman spectra collected, *hypo*-thiophosphate species ($P_2S_6^{4-}$) were indeed present in the samples and the mechanical anisotropy of such species may be accentuated at higher molding pressures, and could explain the shift observed. Nevertheless, corner-sharing and face-sharing configurations differ considerably in activation energies for Li ion conduction 0.25 versus 0.34 eV, respectively. Additionally, the corner-sharing configuration presents about an order of magnitude higher Li diffusivity values compared to the face-sharing configuration (9.2×10^{-8} and 9.6×10^{-9} cm^2 s^{-1} at 300 K and 1 bar, respectively). Further characterization with ^7Li NMR spectroscopy is needed to analyze molecular interactions more thoroughly. Nonetheless, the increase in diffusivity with pressure reaches a limit when the available volume of cation diffusion pathways constrains anion rotational mobility.[36] This is consistent with the calculations performed that showed a diffusion coefficient nearly one order of magnitude lower when pressing LPS glass at a hypothetical pressure of 100×10^2 MPa (Figure 5b). The slight decrease in conductivity of LPS hot-pressed at 360 MPa could be explained by this constriction in anion reorientation[36] and the presence of microcracks in the microstructure resulting in an ionic conductivity of 0.8 mS cm^{-1}.

Additionally, CCD measurements were performed at room temperature as a function of stack pressure (1.5, 3.1, and 6.1 MPa) for cold-pressed LPS, and at 60 °C, 1.5 MPa for both LPS cold-pressed and hot-pressed at 270 MPa (Figures S9, S10, and Table S2, Supporting Information). As it was expected from the outcomes of this work, the sample that was hot-pressed at 270 MPa, with higher ionic conductivity and less volume fraction of porosity (2% compared to 12% for the cold-pressed) exhibited a CCD of 1.1 mA cm^{-2} compared to 0.4 mA cm^{-2} for the cold-pressed sample at 60 °C, 1.5 MPa. Even though the CCD increased by a factor of almost three, the voltage traces of the hot-pressed sample showed significant overpolarization suggesting unstable cycling at the higher current densities (Figure S9c, Supporting Information). The tests performed at different stack pressures elucidated that the overpolarization was a result of loss in contact area due to void formation between the electrode and electrolyte as it has been observed and reported in other systems, such as: Li-argyrodite (Li_6PS_5Cl),[41] Li-LLZO,[42,43] and Na-Na ß'' alumina.[44] Given that Li creep is the dominant mechanism transporting Li to the interface rather than Li diffusion,[41,42] such replenishment can be aided via stack pressure or temperature. In the case of the measurements conducted at room temperature, it was observed that the critical stack pressure (pressure at which the rate of replenishment of Li at the interface is equal to the rate at which Li is depleted from it) was ≥ 3.1 MPa at 0.1 mA cm^{-2}. However, such stack pressure could not be applied to the sample hot-pressed at 270 MPa without fracture given its brittle nature. Hence, the attempt of testing CCD of the hot-pressed sample at a lower stack pressure (1.5 MPa) at 60 °C. It is worth noting that the critical stack pressure is dependent on the current density. Thus, even though Li creep was facilitated by temperature, it was not sufficient to remain below the critical current density for stripping resulting in loss of contact between Li and LPS, leading to increasing local current density for the same overall current density. In other words, the limitation of applying a high enough stack pressure to enable sufficient Li replenishment at the Li-LPS interface upon stripping impeded the measurement of the "real" CCD for plating in this system, which would be expected to be ≥1.1 mA cm^{-2}. These results highlight some of the practical challenges that sulfide-based and other solid electrolytes need to overcome to enable all-solid-state batteries.

3. Conclusion

In this work, it was demonstrated that Li_2S-P_2S_5 75-25 can be densified close to its theoretical density, while preserving the preferred amorphous phase by hot-pressing at the glass transition temperature (≈200 °C) at 180 MPa or above. Through the simultaneous application of pressure at T_{glass} to facilitate plastic flow, but below $T_{crystallization}$ to prevent crystallization, near theoretical density was achieved. Moreover, the distinction between particles and particle boundaries was nearly eliminated at 270 MPa or above, resulting in a material that more closely resembled a melt-processed glass. If it were not for the simultaneous application of pressure above 47 MPa, we believe crystallization would have occurred as we previously demonstrated.[13] It was observed that crystallization was suppressed using pressures ≥ ≈90 MPa at T_{glass} by eliminating particle boundaries and pores that would otherwise act as nucleation sites to promote crystallization of the less desirable thio-LISICON III-analog phase. Even though the metastable crystalline thio-LISICON III analog phase exhibits slightly higher ionic conductivity than the amorphous phase, the presence of grain boundaries may not be desirable as they are known to facilitate Li propagation at higher charging rates.[12] In this study, the application of relatively high pressure (>47 MPa), while heating at T_{glass} resulted in dramatic changes in material properties, such as the mechanical and electrical properties. While changes to the extrinsic properties were observed and analyzed, such as microstructure and relative density, changes to the intrinsic properties, such as *E* and the ionic conductivity were also observed.

The change in *E* was divided in two regimes. One that is distinguished mainly by reduction in the volume fraction of porosity and the other that combines the latter with intermediate-range order changes; rearrangement of atoms at the molecular level leading to a more compact material. The cold-pressed and hot-pressed at 47 and 90 MPa, which observed a slight increase in relative density as a function of molding pressure (3% RD) are in excellent agreement with the exponential relationship between *E* and the volume fraction of porosity described by Rice et al.[23] However, when hot-pressing at 180 MPa and above, changes at the molecular-level may explain the significant increase (>100%) in *E*. The pair distribution functions collected via neutron diffraction with a higher mean coordination number, mostly on the Li–S pairs, suggested a more interconnected arrangement between the Li and S atoms, resulting in higher elastic constants. This is considered a change in intrinsic behavior that we believe is a result of the simultaneous application of pressure and temperature during densification.

This study also showed that LPS hot pressed at 200 °C and 270 MPa with a 98% relative density can attain ionic

conductivities of 1.1 mS cm^{-1} at room temperature with a higher *E* compared to a standard processed cold-pressed sample (360 MPa) with a room temperature ionic conductivity of 0.2 mS cm^{-1}, 89% dense. This conductivity represents the highest room temperature ionic conductivity reported for the LPS 75-25 composition to date. The step increase in ionic conductivity was attributed to a change in Li coordination environment for the sample hot-pressed at 270 MPa, that exhibited the highest value of 1.1 mS cm^{-1} at room temperature. The change between corner-sharing to face-sharing of the Li–S polyhedra with higher diffusivity at 270 MPa found via neutron pair distribution functions and the reduction of the available volume of cation diffusion pathways facilitates the Li ion mobility in the glass structure. Such favorable Li coordination environment and increased diffusivity and mobility explain the step increase in ionic conductivity as a function of molding pressure. Nevertheless, the increase in diffusivity with pressure reaches a limit when the available volume of cation diffusion pathways constrains anion rotational mobility, which we believe it explains the slight decrease in ionic conductivity of the sample hot-pressed at 360 MPa. Interestingly, it was found that the residual stress could play an important role not only on the mechanical integrity of the specimens resulting in an increase in brittleness, but also in ionic transport. The ionic transport behavior observed on the denser microstructures (at and above 1.77 g cm^{-3}, molding pressure of ≥90 MPa) could be explained by the microstructures constructed through ab initio Parrinello–Rahmen dynamics (NPT) at and above 360 MPa, suggesting that even though the EIS measurements were performed at 3.15 MPa, the microstructures resemble the properties of microstructures that are under compression at 360 MPa and above. This was an unexpected result; thus, we believe that the role that residual stress could play on Li transport and consequently in Li electrodeposition should be considered for future studies.

Although it is counterintuitive that a metal, such as Li, that is relatively soft at room temperature,[27,28] could penetrate stiff ceramic solid electrolytes,[45] it has been shown that this is possible at high charging rates.[46] Moreover, pores and particle/grain boundaries are common defects that are believed to play a role in causing ionic current focusing effects or "hot spots," thus influencing stable versus unstable Li electrodeposition.[11,12,47] From this work, it was observed that such defects can be tuned by changing the processing conditions. It was found that *E* is affected by defects, such as pores, but most importantly by molecular arrangements. Moreover, these rearrangements result in a higher diffusivity increasing ionic transport. The outcomes of this work show that optimization of the microstructure of the solid electrolyte likely be intimately connected to the maximum tolerable current density since it can define the resulting defects/properties that have been identified to have an effect on CCD. In addition, the importance of external variables, such as stack pressure and/or temperature to aid Li creep during stripping were identified as practical challenges that sulfide-based solid electrolytes need to overcome to enable all-solid-state batteries. Finally, this work provides insight into processing-structure-property relationships that can be used as a guideline to increase the feasibility of LPS-based all-solid-state battery technology.

4. Experimental Section

Synthesis and Processing: The amorphous $75Li_2S$-$25P_2S_5$ (mol%) solid electrolyte was synthesized from crystalline Li_2S (99.98%, Aldrich) and P_2S_5 (99%, Sigma-Aldrich) by mechanochemical synthesis after being mixed in an agate mortar and pestle. The mixed precursors were placed in a 45-cc zirconia pot with 10 zirconia balls of 10 mm in diameter and 10 zirconia balls of 5 mm in diameter, sealed in a dry Ar-filled glovebox (water concentration below 0.5 ppm), placed inside stainless steel vessels, and transported in an inert atmosphere. The pots were spun at 510 RPM for 10 h in a Planetary Micro Mill (Pulverisette 7, Fritsch GmbH), with 2 h intervals of milling followed by 10 min rest intervals at room temperature.

Milled LPS 75-25 powder was hot-pressed at 200 °C for 4 h between 47 and 360 MPa with a heating rate of 0.7 ± 0.1 °C min^{-1} by resistive heating. Cold-pressed pellets (25 °C) were pressed at 360 MPa for 10 min using a 6 mm diameter stainless steel die in a double-acting configuration.

Glass Transition Determination via TMA: Assignment of the glass transition temperature (T_{glass}) of the cold-pressed LPS specimens was conducted by TMA using (TA Instruments, Q400, 6.07 mm diameter macroexpansion probe) in an Argon atmosphere. Expansion mode was selected, following ASTM Standard Test Method E1545-11 (Reapproved 2016)[48] Cold-pressed specimens were 6 and >2 mm in diameter and thickness, respectively, heated at 0.7 °C min^{-1}—same heating rate used for hot-pressing the samples. No temperature gradients are considered to have affected the data acquired given the slow heating rate used and the thickness of the samples. The TMA specimens were tested using a preload of 0.01 N to ensure good contact between the probe and the specimen. 0.2 N was used as the applied force, and argon as the purge gas (200 mL min^{-1}). To reduce presence of moisture, the TMA instrument chamber was heated at 10 °C min^{-1} to 400 °C for 30 min and cooled down before loading the samples. The intersection of the extrapolation of the slope of the probe displacement curve before and after the transition was used to determine the glass transition temperature.

Crystallization Temperature Determination via DSC: The cold-pressed sample and hot-pressed samples were grounded with an agate mortar and pestle and sealed in aluminum hermetic pans inside a dry (<0.5 ppm H_2O) Ar-filled glovebox. To avoid any residual moisture, the aluminum pans were kept in a vacuum oven at 120 °C. The samples were transferred to the DSC (Q-100, TA Instruments) and heated under flowing nitrogen gas (50 mL min^{-1}) within a temperature range from 40 to 300 °C using a heating rate of 0.7 °C min^{-1}. The zeroline was subtracted from the measured heat flow rate on all samples to get the true sample heat flow rate eliminating influences from apparatus and reference samples, and facilitate analysis of transitions.

Density Determination: Mass densities were obtained by the Archimedes Principle using an Archimedes density determination kit (OHAUS Corp., NJ) inside a dry Ar-filled glovebox. Wet masses were measured with pellets immersed in cyclohexane.

Microstructural Features via SEM: Fractured surfaces of the LPS cold-pressed and hot-pressed bulk specimens were mounted on carbon tape and examined by SEM (JSM-7800F, JEOL) at 15.0 kV using an air-tight transfer vessel (JU2010218, JEOL).

Crystallinity via XRD: Long-range order and identification of the crystalline phases present were determined by analysis of X-ray diffraction patterns (Cu Kα 1.54 Å radiation, step size 0.1°, scan speed of 0.1°2θ min^{-1}) at 40 kV and 15 mA using a diffractometer (Smartlab X-Ray diffractometer, Rigaku). The electrolyte pellets were manually ground in an agate mortar and pestle, and then placed in an air-free holder with a Beryllium window (2455-SH-001, Rigaku) to perform the analysis. The thio-LISICON III XRD pattern adapted from Kanno et al.[19] was digitized by PlotDigitizer 2.6.6.

Elastic Constants from Ultrasonic Velocity Measurements: This technique displaces particles through a material via propagation of a longitudinal or shear wave. For isotropic materials, such as glasses, the two types have distinct values of wave velocity that depend on structural characteristics, such as density and elasticity. Thus, this method can

be used to determine the elastic constants of materials with different structural properties in a nondestructive way.

The samples were prepared following the ASTM E494-15 standard[49] and tested inside of a dry (<0.5 ppm H_2O) Ar-filled glovebox using a pulse-receiver from Olympus (5073PR with M110 and V156 transducers). The couplants used were mineral oil and SWC-2 from Olympus for longitudinal and shear wave speed measurements, respectively. The equations used to determine the elastics constants are as follows

$$V_L = \frac{2 \cdot \Delta x}{\Delta t_L} \tag{1}$$

V_L denotes the longitudinal speed, Δx corresponds to the specimen thickness in which the wave travels through, and Δt_L the time of flight that takes the longitudinal wave to travel the specimen back and forth during a pulse-echo measurement. The same equation is used to determine the shear/transverse wave speed using the corresponding time of flight. The time of flight was measured with an oscilloscope (PicoScope 2207a, Pico Technologies)

$$G = \rho \cdot \nu_s^2 \tag{2}$$

Where G corresponds to the shear modulus, ρ is the density of the material being tested, and versus is the shear/transverse wave speed.

The Young's Modulus was calculated using the equation below

$$E = \frac{\left[\rho \nu_s^2 \left(3\nu_l^2 - 4\nu_s^2\right)\right]}{\left(\nu_l^2 - \nu_s^2\right)} \tag{3}$$

Where ν_L and versus corresponds to the longitudinal and shear wave speed, respectively.

Young's Moduli and Hardness via Nanoindentation: Nanoindentation was performed using a Hysitron 950 Triboindenter using a high-load Berkovich probe. The samples were mounted on magnets (Ted Pella, AFM specimen disks) and polished for surface preparation inside a dry Ar-filled glovebox. Silicon carbide 1200 grit sandpaper was used as initial polishing step, followed by 30, 15, 6, 1, and 0.5 µm diamond pastes against PSA polishing cloths (Mager Scientific). A glass plate along with a custom-made holder were used to maintain flat surfaces, anhydrous cyclohexane was selected to rinse the samples between polishing steps. The samples were transferred to the instrument using air-tight containers, and a thin layer of mineral oil (nonreactive with LPS) was applied onto the samples to protect them from moisture exposure during measurements. The measured values did not change throughout the acquisition period (≈1 h). Thus, validating that the mechanical integrity of the samples was conserved throughout the measurements.

The initial unloading contact stiffness, S, for an axisymmetric indenter, such as a Berkovich probe, the relationship is

$$S = \frac{dP}{dh} = \frac{2}{\sqrt{\pi}} E_r \sqrt{A} \tag{4}$$

Where P denotes the indentation load, h the displacement during one complete cycle of loading and unloading. E_r corresponds to the reduced modulus that accounts for the fact that measured elastic displacement includes contributions from both the specimen and the indenter. The reduced modulus is given by

$$\frac{1}{E_r} = \frac{\left(1 - \nu_f^2\right)}{E_f} + \frac{\left(1 - \nu_i^2\right)}{E_i} \tag{5}$$

Where E_f and ν_f are the elastic modulus and Poisson's ratio of the specimen, and E_i and ν_i are the same quantities for the indenter (Berkovich, Ei = 1140 GPa and ν_i = 0.07). In order to independently establish the hardness and modulus, the projected contact area needs to be measured.[17] The contact areas measured for the cold-pressed sample (360 MPa) and hot-pressed sample at 270 MPa were 8.873 and 6.118 µm^2, respectively

$$H = \frac{P_{max}}{A} \tag{6}$$

Where P_{max} is the peak load and A corresponds to the contact area.

Surface Imaging via AFM: Atomic force microscopy was performed using a Hysitron 950 Triboindenter with in situ imaging capabilities. A PeakForce tapping technique was used, where the maximum load applied was 2 µN. The samples were transferred to the instrument using air-tight containers, and a thin layer of mineral oil (nonreactive with LPS) was applied onto the samples to protect them from moisture exposure during imaging.

EIS Measurements: Symmetric Li|LPS|Li cells were assembled (99.9% metals basis, 750 µm thick, Alfa Aesar) and aligned with a Teflon PTFE tube using nickel pins (99.98% purity, Goodfellow) as current collectors. EIS measurements were acquired on a potentiostat (BioLogic VMP 300) at room temperature under 3.5 MPa (load necessary to minimize the effect of stack pressure on cell impedance). The frequency range used was 50 mHz to 7 MHz using 10 mV as the perturbation voltage and 3 measurements were acquired per frequency. Li metal electrodes were used for ionic conductivity measurements due to inaccessibility to a sputter coater inside an inert atmosphere. Additionally, the ability to achieve low interfacial resistances between Li and LPS allows to clearly identify the contribution of each transport phenomena of the spectra. Since it is known that LPS reacts with Li to form a solid electrolyte interface, measurements were conducted immediately after cell assembly to eliminate Li-LPS contact time as a variable. Furthermore, equivalent circuit modeling was performed to validate the analysis. The equivalent circuit used to analyze frequency-dependent transport phenomena was $Z_u + Q_{Bulk}/Z_{Bulk} + Q_{CT,\ Li\text{-}LPS}/Z_{CT,\ Li\text{-}LPS}$, where Z_u corresponds to the uncompensated impedance, Q_{Bulk} and Z_{Bulk} correspond to the constant phase element and ionic impedance of the bulk, respectively. $Q_{CT,\ Li\text{-}LPS}$ and $Z_{CT,\ Li\text{-}LPS}$ denote the constant phase element and impedance at the electrode/electrolyte interface (CT = charge transfer). The results obtained for the fitting are listed in Table 3. 1.27 cm^2 was the area used for the cold-pressed, hot-pressed at 47 and 90 MPa samples. 0.079 cm^2 was the area used for the samples hot-pressed at 180, 270, and 360 MPa.

High-Resolution PDF: The samples used were synthesized with a 99 at% ^{7}Li enriched mixture for the Li_2S precursor and pressed at the same conditions as the samples with natural Li (92.5 at% ^{7}Li, 7.5 at% ^{6}Li). The samples were ground into powder using an agate mortar and pestle and sealed in quartz capillaries (2 mm in diameter, 0.01 mm for the wall thickness, Hampton Research, ≈60 mm^3 of sample) in a dry (<0.5 ppm H_2O) Ar-filled glovebox. The measurements were carried out at 380 K using the Nanoscale-Ordered Materials Diffractometer (NOMAD) at Oak Ridge National Laboratory, Spallation Neutron Source. The data were reduced and corrected for attenuation and multiple scattering using ADDIE (ADvanced Diffraction Environment) user software.

Raman Spectroscopy: Raman spectra were collected using a Horiba instrument (LabRAM HR-800, Horibausing). A 532 nm laser was used, spot size of 50 µm. Samples were loaded and sealed in a quartz window holder custom-made inside of a dry Ar-filled glovebox.

Computational Methods: AIMD were conducted to study the structure and diffusivity of amorphous Li_3PS_4. The initial amorphous structure with Li^+ and tetrahedral PS_4^{3-} ionic units was generated via a Monte Carlo approach[50] with periodic boundary conditions at a density of 1.88 g cm^{-3}; followed by a AIMD melt-and-quench routine. The structure was heated to 1000 K at 70 K ps^{-1}, held at 1000 K for 3 ps, then cooled at the same rate with an additional 3 ps of equilibration at the target temperature. The simulation cell consisted of 60 Li^+ and 20 PS_4^{3-} ions. Calculations were performed using the Vienna ab initio simulation package.[51] The generalized gradient approximation in the formulation of Perdew–Burke–Emzerhof was used in combination with the projector augmented method.[52,53] Lithium trajectories were propagated with a 2 fs time step within the isothermal-isobaric (NPT) ensemble, employing the Langevin thermostat.[15] The plane-wave energy cutoff was

set to 400 eV and a single k-point was used. Lithium diffusivities were evaluated using the Einstein relation

$$D = \frac{1}{6tN}\sum_{i}^{N}\left\langle \left| r_i\left(t+t'\right) - r_i\left(t'\right)\right|^2 \right\rangle, \tag{7}$$

Where $\mathbf{r}_i(t)$ is the position of the i_{th} lithium ion, N is the number of lithium ions, and the enclosing brackets $\cdots$ indicate an average over the time interval t. The diffusivity was calculated at temperatures of 700, 850, and 1000 K; and at pressures of 0.1, 360, 1000, 2000, and 100×10^2 MPa.

The elastic properties of amorphous Li_3PS_4 subject to hydrostatic pressure were calculated with density functional theory using the stress–strain approach.[54] The amorphous simulation cell exhibited triclinic symmetry, which requires the calculation of 21 independent elastic coefficients C_{ij}. The stresses resulting from the application of six finite strains with displacements of ±0.015 Å were used to solve for C_{ij} in $\sigma_i = C_{ij}\,\varepsilon_j$ $(i, j = 1, 2, \ldots, 6)$. The force and electronic convergence were set to 10^{-4} eV Å^{-1} and 10^{-6} eV, respectively. The bulk, shear, and Young's moduli were subsequently determined using the Voigt-Reuss-Hill approximation. This approximation relates the single-crystal elastic constants to the polycrystalline elastic moduli.[55] The Voigt (V) moduli provide an upper bound to these values, the Reuss (R) moduli provides a lower bound, and the Hill (H) moduli is the arithmetic average of the two. The bulk B and shear modulus G within these approximations are defined as

$$B_V = \frac{\left(C_{11}+C_{22}+C_{33}+2\left(C_{12}+C_{23}+C_{31}\right)\right)}{9} \tag{8}$$

$$B_R = \frac{1}{\left(S_{11}+S_{22}+S_{33}+2\left(S_{12}+S_{23}+S_{31}\right)\right)} \tag{9}$$

$$B_H = \frac{\left(B_V + B_R\right)}{2} \tag{10}$$

$$G_V = \frac{\left(C_{11}+C_{22}+C_{33}-C_{12}-C_{23}-C_{31}+3\left(C_{44}+C_{55}+C_{66}\right)\right)}{15} \tag{11}$$

$$G_R = \frac{15}{\left(4\left(S_{11}+S_{22}+S_{33}\right)-4\left(S_{12}+S_{23}+S_{31}\right)+3\left(S_{44}+S_{55}+S_{66}\right)\right)} \tag{12}$$

$$G_H = \frac{\left(G_V + G_R\right)}{2} \tag{13}$$

where $S = C^{-1}$ is the compliance matrix and the subscripts refer to either the Voigt, Reuss, or Hill moduli. Finally, the Young's modulus E and Poisson's ratio ν are determined by

$$E = \frac{9BG}{3B+G},\ \nu = \frac{\left(3B-2G\right)}{2\left(3B+G\right)} \tag{14}$$

The Voight-Reuss-Hill approximation is ideal for an amorphous material since the approach averages all methods over all possible lattice orientations.[55] Given that there is no directionality in amorphous materials, this approach is best suited for LPS in this work.

An analysis of the connectivity of void/pore space within Li_3PS_4 glass that is available for Li+ migration was obtained via Voronoi network analysis (Zeo++ code).[56] Ionic radii were adopted as the effective sizes for each elemental component.[57]

Supporting Information

Supporting Information is available from the Wiley Online Library or from the author.

Acknowledgements

A portion of this research was conducted at ORNL's Spallation Neutron Source, a DoE Office of Science User Facility operated by the Oak Ridge National Laboratory. In addition, a portion of this research was sponsored by Toyota Research Institute of North America, Toyota Motor Engineering & Manufacturing North America Inc. R.G.M. and J.S. would like to thank Tim S. Arthur for valuable discussions and Raman spectra acquisition.

Conflict of Interest

The authors declare no conflict of interest.

Author Contributions

Conceptualization, R.G.M. and J.S. Experimental data acquisition and analysis, R.G.M. and J.S. Theoretical calculations, J.G.S. and D.J.S. Computational data analysis, R.G.M., J.G.S., D.J.S., and J.S. Pair distribution functions acquisition and analysis, R.G.M. J.G.S. and J.C.N. All authors contributed to writing - review & editing.

Keywords

elastic properties, glassy solid electrolytes, ionic transport, solid-state batteries, sulfide-based solid electrolytes

Received: January 24, 2020
Revised: February 21, 2020
Published online: April 1, 2020

[1] S. Chu, A. Majumdar, *Nature* **2012**, *488*, 294.
[2] J. A. Lewis, J. Tippens, F. J. Q. Cortes, M. T. McDowell, *Trends Chem.* **2019**, *1*, 845.
[3] B. D. McCloskey, *J. Phys. Chem. Lett.* **2015**, *6*, 4581.
[4] P. Albertus, S. Babinec, S. Litzelman, A. Newman, *Nat. Energy* **2018**, *3*, 16.
[5] A. Manthiram, X. Yu, S. Wang, *Nat. Rev. Mater.* **2017**, *2*, 16103.
[6] Z. Liu, W. Fu, E. A. Payzant, X. Yu, Z. Wu, N. J. Dudney, J. Kiggans, K. Hong, A. J. Rondinone, C. Liang, *J. Am. Chem. Soc.* **2013**, *135*, 975.
[7] A. Sakuda, A. Hayashi, S. Hama, M. Tatsumisago, *J. Am. Ceram. Soc.* **2010**, *93*, 765.
[8] K. Minami, F. Mizuno, A. Hayashi, M. Tatsumisago, **2007**, *178*, 837.
[9] S. Ito, M. Nakakita, Y. Aihara, T. Uehara, N. Machida, *J. Power Sources* **2014**, *271*, 342.
[10] A. Hayashi, K. Minami, S. Ujiie, M. Tatsumisago, *J. Non-Cryst. Solids* **2010**, *356*, 2670.
[11] L. Porz, T. Swamy, B. W. Sheldon, D. Rettenwander, T. Frömling, H. L. Thaman, S. Berendts, R. Uecker, W. C. Carter, Y.-M. Chiang, *Adv. Energy Mater.* **2017**, *7*, 1701003.
[12] E. J. Cheng, A. Sharafi, J. Sakamoto, *Electrochim. Acta* **2017**, *223*, 85.
[13] R. Garcia-Mendez, F. Mizuno, R. Zhang, T. S. Arthur, J. Sakamoto, *Electrochim. Acta* **2017**, *237*, 144.
[14] A. Sakuda, A. Hayashi, M. Tatsumisago, *Sci. Rep.* **2013**, *3*, 2261.
[15] I. S. Gutzow, *The Vitreous State: Thermodynamics, Structure, Rheology, and Crystallization*, Springer, New York **2013**.
[16] A. Hayashi, S. Hama, F. Mizuno, K. Tadanaga, T. Minami, M. Tatsumisago, *Solid State Ionics* **2004**, *175*, 683.
[17] M. W. Barsoum, *Fundamentals of Ceramics*, IOP, Bristol **2003**.
[18] A. Sakuda, A. Hayashi, Y. Takigawa, K. Higashi, M. Tatsumisago, *J. Ceram. Soc. Jpn.* **2013**, *121*, 946.

[19] R. Kanno, M. Murayama, *J. Electrochem. Soc.* **2001**, *148*, A742.
[20] H. A. A. Sidek, S. P. Chow, Z. A. Talib, S. A. Halim, *Solid State Sci. Technol.* **2003**, *11*, 7.
[21] A. Kato, M. Nose, M. Yamamoto, A. Sakuda, A. Hayashi, M. Tatsumisago, *J. Ceram. Soc. Jpn.* **2018**, *126*, 719.
[22] *CRC Handbook of Chemistry and Physics: A Ready-Reference Book of Chemical and Physical Data* (Eds: W. M. Haynes, D. R. Lide), CRC Press, Boca Raton, FL **2013**.
[23] R. W. Rice, *Porosity of Ceramics*, M. Dekker, New York **1998**.
[24] T. Rouxel, *J. Am. Ceram. Soc.* **2007**, *90*, 3019.
[25] K. Ohara, A. Mitsui, M. Mori, Y. Onodera, S. Shiotani, Y. Koyama, Y. Orikasa, M. Murakami, K. Shimoda, K. Mori, T. Fukunaga, H. Arai, Y. Uchimoto, Z. Ogumi, *Sci. Rep.* **2016**, *6*, 21302.
[26] F. C. Serbena, E. D. Zanotto, *J. Non-Cryst. Solids* **2012**, *358*, 975.
[27] R. Messer, F. Noack, *Appl. Phys.* **1975**, *6*, 79.
[28] F. Hao, A. Verma, P. P. Mukherjee, *ACS Appl. Mater. Interfaces* **2018**, *10*, 26320.
[29] A. Masias, N. Felten, R. Garcia-Mendez, J. Wolfenstine, J. Sakamoto, *J. Mater. Sci.* **2019**, *54*, 2585.
[30] A. Hayashi, S. Hama, T. Minami, M. Tatsumisago, *Electrochem. Commun.* **2003**, *5*, 111.
[31] A. Hayashi, S. Hama, H. Morimoto, M. Tatsumisago, T. Minami, *J. Am. Ceram. Soc.* **2001**, *84*, 477.
[32] F. Mizuno, A. Hayashi, K. Tadanaga, M. Tatsumisago, *Adv. Mater.* **2005**, *17*, 918.
[33] K. Homma, M. Yonemura, T. Kobayashi, M. Nagao, M. Hirayama, R. Kanno, *Solid State Ionics* **2011**, *182*, 53.
[34] M. Tachez, J.-P. Malugani, R. Mercier, G. Robert, *Solid State Ionics* **1984**, *14*, 181.
[35] A. Orera, F. García-Alvarado, J. T. S. Irvine, *Chem. Mater.* **2007**, *19*, 2310.
[36] J. G. Smith, *Ph.D. Thesis*, University of Michigan, XXXX **2018**.
[37] C. Dietrich, D. A. Weber, S. J. Sedlmaier, S. Indris, S. P. Culver, D. Walter, J. Janek, W. G. Zeier, *J. Mater. Chem. A* **2017**, *5*, 18111.
[38] K. Ichihashi, D. Konno, T. Date, T. Nishimura, K. Yu. Maryunina, K. Inoue, T. Nakaya, K. Toyoda, Y. Tatewaki, T. Akutagawa, T. Nakamura, S. Nishihara, *Chem. Mater.* **2018**, *30*, 7130.
[39] N. F. Mott, R. W. Gurney, *Electronic Processes in Ionic Crystals*, Clarendon Press, Oxford **1953**.
[40] H. Chen, T. Hong, Y. Jing, *J. Alloys Compd.* **2020**, *819*, 152950.
[41] J. Kasemchainan, S. Zekoll, D. Spencer Jolly, Z. Ning, G. O. Hartley, J. Marrow, P. G. Bruce, *Nat. Mater.* **2019**, *18*, 1105.
[42] M. J. Wang, R. Choudhury, J. Sakamoto, *Joule* **2019**, *3*, 2165.
[43] T. Krauskopf, H. Hartmann, W. G. Zeier, J. Janek, *ACS Appl. Mater. Interfaces* **2019**, *11*, 14463.
[44] D. Spencer Jolly, Z. Ning, J. E. Darnbrough, J. Kasemchainan, G. O. Hartley, P. Adamson, D. E. J. Armstrong, J. Marrow, P. G. Bruce, *ACS Appl. Mater. Interfaces* **2020**, *12*, 678.
[45] S. Yu, R. D. Schmidt, R. Garcia-Mendez, E. Herbert, N. J. Dudney, J. B. Wolfenstine, J. Sakamoto, D. J. Siegel, *Chem. Mater.* **2016**, *28*, 197.
[46] M. Wang, J. B. Wolfenstine, J. Sakamoto, *Electrochim. Acta* **2019**, *296*, 842.
[47] F. Shen, M. B. Dixit, X. Xiao, K. B. Hatzell, *ACS Energy Lett.* **2018**, *3*, 1056.
[48] *ASTM E1545-00, Standard Test Method for Assignment of the Glass Transition Temperature by Thermomechanical Analysis*, ASTM International, West Conshohocken, PA **2000**.
[49] *ASTM E494-15, Standard Practice for Measuring Ultrasonic Velocity in Materials*, ASTM International, West Conshohocken, PA **2015**.
[50] R. L. C. Akkermans, N. A. Spenley, S. H. Robertson, *Mol. Simul.* **2013**, *39*, 1153.
[51] G. Kresse, J. Furthmüller, *Phys. Rev. B* **1996**, *54*, 11169.
[52] J. P. Perdew, K. Burke, M. Ernzerhof, *Phys. Rev. Lett.* **1996**, *77*, 3865.
[53] P. E. Blöchl, *Phys. Rev. B* **1994**, *50*, 17953.
[54] K. Hirota, Z.-G. Ye, S. Wakimoto, P. M. Gehring, G. Shirane, *Phys. Rev. B* **2002**, *65*, 104105.
[55] R. Yokoyama, J. Harada, *Nihon Kessho Gakkaishi* **2010**, *52*, 113.
[56] T. F. Willems, C. H. Rycroft, M. Kazi, J. C. Meza, M. Haranczyk, *Microporous Mesoporous Mater.* **2012**, *149*, 134.
[57] R. D. Shannon, *Acta Crystallogr. A* **1976**, *32*, 751.